Journal of Catalysis **188,** 353–364 (1999)
Article ID jcat.1999.2676, available online at http://www.idealibrary.com on IDEAL®

Spectroscopic Characterization and Catalytic Activity of Zeolite X Containing Occluded Alkali Species

Eric J. Doskocil and Robert J. Davis[1]

Department of Chemical Engineering, University of Virginia, Charlottesville, Virginia 22903–2442

Received June 4, 1999; accepted August 17, 1999

Samples of zeolite X containing occluded cesium oxide (prepared via decomposition of impregnated cesium acetate) and occluded alkali metal (prepared via decomposition of impregnated alkali azide) were synthesized, characterized, and tested as solid base catalysts. X-Ray absorption spectroscopy at the Cs L_{III} edge was used to probe the local structure in zeolites containing exchangeable cesium cations and occluded cesium oxides. Since the Cs–O interatomic distances determined by EXAFS were similar in both the zeolites and reference compounds, the white line intensity was proposed to correlate with ionicity of the Cs–O bond. Infrared spectroscopy of adsorbed carbon dioxide and temperature-programmed desorption of CO_2 confirmed that occlusion of cesium oxide in the zeolite pores created new strong base sites that were catalytically active in the decomposition of 2-propanol to acetone. Alkali metal-loaded zeolites were found to be catalysts for the side-chain alkenylation of *o*-xylene with 1,3-butadiene to form 5-*o*-tolyl-2-pentene. Results from ESR spectroscopy suggested that extralattice alkali metal clusters contribute to the formation of active species for alkenylation.

INTRODUCTION

Solid acids have received significant attention in the literature due to their industrial importance in replacing liquid acids in petroleum processing. However, very little work has been done to elucidate the nature of the active sites on solid base materials, despite their potential as important industrial catalysts. Interest in solid basicity began shortly after Pines and colleagues' early investigations of sodium metal-doped alumina as a strong base catalyst (1). More recently, research has aimed at understanding how to produce strong solid base catalysts that are effective for reactions such as double-bond isomerization of olefins, side-chain alkylation of aromatics, dehydrogenation of alcohols, and Knoevenagel condensation of aldehydes (2–6).

Both rubidium and cesium oxide have been reported to be "superbases," possessing a Hammett basicity function exceeding +26 (7). These oxides have a very low surface area, which limits their ability to be effective catalysts. Therefore, it is believed that supporting these oxides on high-surface-area carriers would give materials with strong basicity as well. Because cesium has been shown to create stronger basic centers than other alkali metals in Group IA, much attention in the literature has focused on supported cesium catalysts.

Zeolites that have been modified by ion exchange of alkali cations have emerged as interesting solid bases. They are known to catalyze reactions that require a base site, like toluene alkylation with methanol. The base strength of alkali ion-exchanged zeolites increases with increasing electropositivity of the exchange cation. Occlusion of alkali oxide clusters in zeolite cages via decomposition of impregnated alkali salts results in a further increase in the basicity of these materials (2, 4, 8, 9–12). A majority of these catalysts are produced via decomposition of a supported alkali precursor in the cages of a zeolite after incipient wetness impregnation of a solution containing the precursor. Although a significant contribution to the understanding of base catalysts involving supported alkali species has already been achieved, the nature of the occluded alkali species has been elusive, with the actual form of the occluded oxide still in question. Recently, NMR spectroscopy has been used to determine the location of cesium species in excess of ion-exchange capacity (13, 14). In addition, results from NMR experiments on a variety of alkali oxides, superoxides, and peroxides suggest that the peroxide and superoxide phases should be considered for their possible role in catalytic reactions as both a base and an oxidant (15).

Recently, zeolites that contain alkali metals in the pores have been investigated as high-strength solid base catalysts. A novel preparation technique has been introduced in which alkali metal clusters are prepared via the decomposition of alkali metal azides in the presence of a zeolite (16–22). Unlike their alkali metal counterparts, the azides themselves are stable in normal atmosphere. The catalytic properties of zeolite-supported azides containing ionic and/or metal clusters of alkali have been investigated using the isomerization of 1-butene (16, 17, 21). Decomposition of the alkali azide in the pores of the zeolite has been

[1] To whom correspondence should be addressed.

0021-9517/99 $30.00

determined to form either ionic or neutral alkali metal clusters, depending primarily on the heating rate used to decompose the supported azide; fast heating rates ($\sim$25 K min^{-1}) result in ionic clusters while slow heating rates ($\sim$1 K min^{-1}) give primarily neutral metal clusters (17). Since either of the alkali clusters mentioned can be formed on introduction of an alkali metal into a zeolite, it is important to determine the actual state of the alkali when studying its role in reactivity. Electron spin resonance (ESR) spectroscopy has been used to determine whether alkali metal or ionic clusters are present in the cages of various X and Y zeolites (17–19, 23, 24).

The side-chain alkenylation of *o*-xylene with 1,3-butadiene to produce 5-*o*-tolyl-2-pentene (OTP) requires a very strong base and has been carried out in the liquid phase over pure sodium and potassium metal suspended in a solution of *o*-xylene (25–29). In addition, many catalysts have been investigated that use an alkali metal supported on a basic carrier, including alkaline earth oxides (27, 30), base-promoted alumina (28, 29, 31), and zeolites (26). The formation of OTP is the first step in the production of polyethylene naphthalate (PEN), a polyester that has the potential to be an important new entrant in the plastics market due to its increased rigidity, strength, heat stability, and barrier properties compared with polyethylene terephthalate (PET) (32). Both *trans* and *cis* isomers of OTP can be formed from the alkenylation of *o*-xylene. For the preparation of the PEN monomer, the *trans* form is the desired structure for intramolecular cyclization to the naphthalene derivative, which is required later in processing (26). The mechanism for this reaction is similar to that observed for side-chain alkylations and alkenylations of alkylbenzenes using both mono-olefins (33–36) and diolefins (37, 38).

For alkali-modified zeolites, little is understood about the interaction between the zeolite and the occluded alkali species, whether it be an alkali oxide or a metal cluster. In this paper, we have used X-ray absorption spectroscopy at the cesium L_{III} edge in an attempt to probe the local environment around cesium exchanged and occluded in zeolites. Fourier transform infrared (FT-IR) spectroscopy was also used to determine the adsorption modes of carbon dioxide on alkali-exchanged zeolites, with and without occluded cesium oxide. In addition, the effect of occluded cesium oxide on the rate of 2-propanol decomposition was investigated. Finally, we studied strong base catalysts containing supported alkali metals prepared via decomposition of an occluded alkali azide on X zeolite. The form of alkali obtained from azide decomposition in the zeolite cages was investigated using electron spin resonance spectroscopy. These alkali metal-containing zeolites were then tested in the liquid-phase side-chain alkenylation of *o*-xylene with 1,3-butadiene to form 5-*o*-tolyl-2-pentene.

METHODS

Synthesis of Alkali-Modified Zeolites

Potassium- and cesium-exchanged zeolites were obtained by triply ion-exchanging NaX (Union Carbide, Lot No. 943191060078, or UOP, Lot no. 07483-36) in 1 M solutions of potassium nitrate (Mallinckrodt, reagent grade) and cesium acetate (Aldrich 99.9%), respectively. The exchanged samples were then washed with an aqueous solution of the corresponding alkali hydroxide (pH 13.3), unless otherwise noted. The exchanged samples were contacted with distilled, deionized water in an attempt to remove excess alkali that might have been occluded in the zeolite cages during ion exchange. The resultant ion-exchanged materials were dried overnight in air at 373 K. The zeolites were then heated in flowing air at 4 K min^{-1} (BOC Gases) to 773 K and subsequently held at that temperature for 10 h. If a sample were to be subsequently impregnated with excess cesium acetate, it was first placed in a high-humidity vessel to slowly reintroduce water to the zeolite before impregnation with an aqueous solution of the appropriate concentration. The impregnated catalyst was then calcined in an identical manner to the ion-exchanged materials to decompose the occluded acetate. The zeolites containing occluded cesium oxide contained between 1 and 11 excess Cs atoms per unit cell. If the ion-exchanged zeolite were to be loaded with an azide precursor after heat treatment, it was first placed in a methanol atmosphere at room temperature to slowly introduce methanol. Enough sodium azide (Aldrich, 99%) or cesium azide (Acros, 80–90 wt%, remainder 10–20% methanol) to prepare a catalyst with a known number of alkali metal atoms per supercage was dissolved in about 15 cm^3 of methanol under stirring. The zeolite ($\sim$10 g) was subsequently added to the solution while stirring. The mixture was stirred under an atmosphere of flowing dinitrogen to slowly evaporate the methanol. The resultant powder was dried overnight in air at 373 K. Thermal decomposition of the azide-loaded zeolites was performed immediately prior to any reaction or spectroscopic investigation since the resulting alkali metal clusters were unstable under normal atmosphere. Dinitrogen and argon adsorption isotherms were obtained on a Coulter Omnisorp 100CX. Pore volumes were obtained by determining the amount of liquid adsorbed at a relative pressure (P/P_0) of 0.3. Elemental analysis of the alkali-exchanged zeolites was performed by Galbraith Laboratories, Knoxville, Tennessee.

X-Ray Absorption Spectroscopy

X-Ray absorption spectra were recorded at the Cs L_{III} edge (5014 eV) on beam line X19A at the National Synchrotron Light Source, Brookhaven National Laboratory (Upton, NY), in the transmission mode of data collection. The storage ring operated with an electron energy

of 2.54 GeV with currents ranging from 100 to 300 mA. Higher harmonics in the beam were rejected by detuning the Si(111) monochromator crystals to give 75% of the maximum intensity. The first ionization chamber was filled with pure He to achieve high photon flux to the sample. The I_t and I_{ref} ionization chambers were filled with pure N_2 to optimize sensitivity. The *K* edge of titanium (4966 eV) was used for energy calibration.

Each cesium-containing sample consisted of a hand-pressed self-supporting wafer of catalyst mixed with boron nitride (Alfa, 99.5%) to adjust absorption, and was loaded into an *in situ* cell capable of heating in a helium (grade 6, ultrahigh purity) atmosphere. Cesium compounds ["Cs_2O" (Aldrich, total metallic impurities <1%), Cs_2CO_3 (Aldrich, 99.995%), $Cs_2C_2O_4$ (Aldrich), CsOAc (Aldrich, 99.995%), $CsOH \cdot H_2O$ (Aldrich, <5% Cs_2CO_3), $CsHCO_3$ (Alfa–Aesar, 99.99%) and CsOOCH (Alfa–Aesar, 99.9%)] were compressed with boron nitride between two Kapton windows in a controlled dinitrogen atmosphere to minimize exposure of the air-sensitive compounds to dioxygen and water.

The EXAFS data were processed with Macintosh versions of the University of Washington analysis programs. Curve fitting was performed in the *k*-space region 1.95–6.95 $Å^{-1}$. Bulk cesium oxide, which is a mixture of oxides with an average empirical formula claimed to be Cs_2O, was used as a reference material for fitting the EXAFS functions of the samples. However, cesium fluoride (Aldrich, 99.99%), with its well-defined rock salt crystal structure (Cs–F distance of 3.00 Å and coordination number of 6) was used to determine the Cs–O distance in the commercial "Cs_2O" sample (39). The backscattering potential (phase shift) for fluorine was assumed to be identical to that of oxygen for the determination of the Cs–O distance for the commercial cesium oxide sample. Cesium fluoride has been used as an EXAFS standard in the investigation of cesium crown ethers (40). We found an average Cs–O distance of 2.95 Å in the commercial cesium oxide. This EXAFS-extracted interatomic distance was between the two values reported in the literature (41, 42) and was the same as the Cs–O distance found in Cs_2O_2 (43).

Fourier Transform Infrared Spectroscopy

The *in situ* FT-IR spectra were collected using a Bio-Rad FTS-60A spectrometer in transmission mode with a resolution of 2 cm^{-1}. All samples were treated in a stream of flowing helium (BOC Gases, Grade 5) that was passed through a Supelco OMI-2 purifier used to remove trace contaminants. The sample pellet was heated at the rate of 4 K min^{-1} to 773 K and held at that temperature for 10 h before cooling to 373 K. Carbon dioxide was then introduced to the helium stream in about a 1 : 1 ratio of CO_2 to He for 20 min to allow for CO_2 adsorption. After purging the system with helium for about 30 min, a sample spectrum was recorded. The temperature was increased in 100 K increments and sample spectra were recorded until no adsorbed carbon dioxide species were observed on the catalyst surface.

Decomposition of 2-Propanol

Decomposition of 2-propanol was carried out in a quartz U-tube continuous-flow fixed-bed reactor which contained a quartz frit used to support the catalyst. An empty reactor at 563 K showed no conversion to acetone and negligible production of propene. Between 0.1 and 0.2 g of size-separated (+40/−60) fresh catalyst was heated at 4 K min^{-1} to 773 K in flowing helium (BOC gases, grade 5) and held at that temperature for 10 h. The catalyst bed was then cooled to 563 K prior to reaction. Reactant 2-propanol, dried over 3A molecular sieves (Davidson Chemical), was continuously fed by a syringe pump to give a vapor stream consisting of a 1 : 9 molar ratio with the helium carrier gas. The reaction was run at differential conversion (∼1%). The product composition was determined by gas chromatography on a Hewlett–Packard HP-5890 fitted with an Alltech Carbowax column. The selectivity is defined as the rate of acetone production divided by the overall rate of 2-propanol consumption. By-products were detected at initial reaction times, but disappeared after about 2 h on stream.

Electron Spin Resonance Spectroscopy of Azide-Modified Zeolites

Preparation of samples for analysis using ESR spectroscopy was performed in a U-shaped quartz tube containing a quartz frit to support the sample. Each catalyst sample was size separated (+40/−60) to facilitate transfer into a Spectrosil quartz ESR tube attached to the U-shaped tube. Between 0.80 and 0.95 g of sample was loaded into the U-tube and dinitrogen (grade 5, BOC) was passed through the sample for at least 2 h to purge air from the apparatus. Afterward, the sample was heated *in vacuo* in the following manner: 1 K min^{-1} to 308 K, 1.4 K min^{-1} to 523 K, 1.5 h at 523 K, 1 K min^{-1} to 773 K, and 7.0 h at 773 K. The ultimate pressure reached at 773 K was less than 1.0×10^{-6} mbar for each sample. A thin-film ring of alkali metal condensed on the interior of the U-tube above the opening of the furnace after heating. After treatment, the sample was loaded into the ESR tube by inverting the U-tube to fill the tube with sample. The tube was hermetically sealed under vacuum with a torch.

Electron spin resonance studies were performed on a Varian E-line Century Series EPR spectrometer. All samples were analyzed at room temperature at a magnetic field modulation of 100 kHz, a microwave power near 2 mW, and a microwave frequency about 9.465 GHz. A standard sample of 2,2-diphenyl-1-picrylhydrazyl (DPPH) physically mixed with NaX, assigned a *g* value of 2.0036, was used to determine the *g* values of the central lines in the samples.

Side-Chain Alkenylation of o-Xylene with 1,3-Butadiene

The side-chain alkenylation of liquid-phase *o*-xylene with 1,3-butadiene was carried out in a semi-batch reactor fitted with a condenser and loaded with about 0.5 g of size-selected (+40/−60) fresh supported azide catalyst. First, a flowing dinitrogen stream of about 30 cm^3 min^{-1} (BOC, grade 5) was dried over 3A molecular sieves and passed over the catalyst for about 2 h prior to thermal treatment to purge oxygen, water, and carbon dioxide from the reactor. The catalyst was heat treated under flowing dinitrogen in a manner identical to that mentioned previously for the ESR studies. The temperature was lowered below 416 K, after which 10 cm^3 of *o*-xylene was added slowly while stirring. The reaction mixture was allowed to stir while refluxing at 416–418 K for about 1 h. The reaction was initiated by bubbling a dilute stream of 1,3-butadiene (Aldrich, 99+%) at a rate of about 1.8 cm^3 min^{-1} through the *o*-xylene/catalyst mixture in a 9 : 1 ratio of dinitrogen to 1,3-butadiene. By using such a dilute stream, oligomerization of butadiene was reduced. Liquid samples were taken periodically (about every 1.5 h) to monitor the progress of the reaction.

The solution remained colorless when the catalyst was stirred in refluxing *o*-xylene. However, after initiating flow of 1,3-butadiene through the solution, the solution turned dark red when conversion to OTP was detected. The red solution color was also reported by Eberhardt and Peterson for both Na and K metal supported on CaO (30). The dark red solution was also observed when pure K metal was suspended in *o*-xylene. Observation of the red color likely indicated the presence of an organoalkali species present in solution. After filtration through an Acrodisc 13 CR PTFE (0.45-μm) syringe filter, the liquid sample was colorless. Reaction samples were analyzed using an Alltech Heliflex AT-1301 capillary column on a Hewlett–Packard HP-5890 gas chromatograph with a flame ionization detector. Confirmation of OTP product formation, as well as the retention times of mono-, di-, and trialkenylated products, was determined by mass spectrometry of the reaction product using a Hewlett–Packard HP-6890 gas chromatograph/mass spectrometer.

RESULTS AND DISCUSSION

XANES and EXAFS at the C L_{III} Edge

The compositions of samples used for X-ray absorption spectroscopy can be found in Table 1. Based on the amount of Na originally present in the zeolite, the CsX zeolite was 61% exchanged. The potassium-exchanged zeolite X was loaded with about six occluded cesium atoms per unit cell. The absorption edge for each of the bulk compounds ("Cs_2O," Cs_2CO_3, $Cs_2C_2O_4$, CsOAc, $CsOH \cdot H_2O$, Cs_2CO_3, $CsHCO_3$, CsOOCH) occurred at the same energy as expected for the 1+ formal oxidation state each of these samples share. Similarly, the absorption edge for the Cs-containing zeolite catalysts also occurred at this energy, confirming the formal oxidation state of cesium in these samples to be 1+.

TABLE 1

Properties of Cesium-Modified Catalysts Studied by X-Ray Absorption Spectroscopy

Catalyst	Composition	Pore volume (cm^3 Ar g^{-1})
CsX	$H_{1.1}Na_{38.8}Cs_{47.8}Al_{87.7}Si_{104.3}O_{384}$	0.119
CsO_x/KX	$Na_{4.3}K_{87.4}Cs_{6.0}Al_{87.7}Si_{104.3}O_{384}$	0.138

The white line intensity at the Cs L_{III} edge for the bulk compounds and zeolite catalysts was determined by measuring the peak height for each normalized XANES spectrum. A comparison of XANES results for representative samples is presented in Fig. 1 and the ratio of the white line intensity of a sample to that of Cs_2CO_3 is summarized in Table 2. The CsX zeolite exhibited higher white line intensity than any of the other compounds. The most intense white line occurred for the zeolite containing cesium introduced via impregnation.

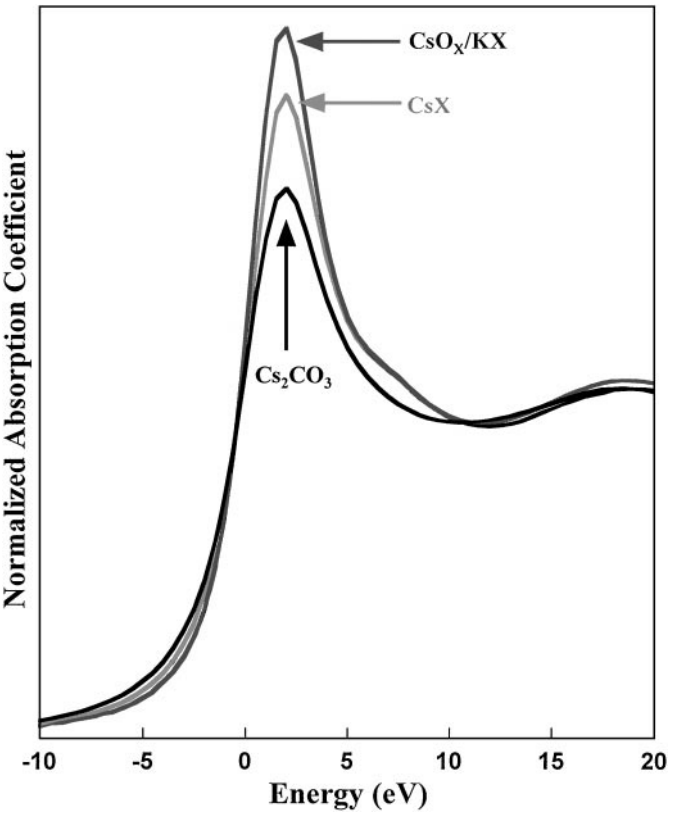

FIG. 1. Cs L_{III} edge spectra for CsO_x/KX, CsX, and Cs_2CO_3 at room temperature. The zero in energy corresponds to the L_{III} edge observed for the cesium oxide standard.

TABLE 2

White Line Intensity Ratios of Cesium Catalysts and Compounds to a Cesium Carbonate Reference

Cesium sample	White line ratio, sample : Cs_2CO_3
$Cs_2C_2O_4$	0.99
Cs_2CO_3	1.00
$CsHCO_3$	1.04
Cs_2O	1.29
$CsOH \cdot H_2O$	1.33
CsOAc	1.35
CsX	1.42
CsO_x/KX	1.73

The Cs L_{III} edge corresponds to the excitation of a $2p_{3/2}$ electron into unoccupied states of *s*- and *d*-type symmetry. The higher the intensity of this "white line" transition, the lower the ground-state electron occupation of the low-lying vacant states associated with cesium. For Cs, the edge structure is likely to be dominated by the unoccupied 6*s* states. However, a density functional theory study of a Cs–O dimer revealed that the highest occupied molecular orbital is formed by the overlap of an O 2*p* orbital with that of Cs 5*d* orbital. Thus, Cs atoms that are highly highly coordinated to oxygen may also have a smaller L_{III} edge feature due to fewer available 5*d* states around Cs. Nevertheless, as long as the Cs–O interatomic distance is identical (see below), the white line intensity should correlate with the ionicity of the Cs–O bond which decreases the *s*-type orbital population near Cs. Both the impregnated and ion-exchanged cesium zeolites had a more intense white line than any of the cesium compounds, indicating that the Cs–O interaction in the zeolites is more ionic than in the bulk-phase compounds.

The EXAFS region of the X-ray absorption spectra was complicated by the presence of a double excitation about 100 eV above each of the Cs *L* edges (40, 44–47). This excitation has been observed for many of the ions in the Xe-isoelectronic series (i.e., Cs^+, Ba^{2+}, La^{3+}) (46). The double excitation in the EXAFS region complicates the extraction of structural data from the spectrum. Kodre *et al.* have determined the excitation contribution to be a fraction of the white line intensity for each of the Xe-like ions, enabling the effect of the excitation to be removed before extracting interatomic distances, coordination numbers, and Debye–Waller factors (46) from the EXAFS. In our analysis, we used the MacEXAFS deglitching routine to fit a spline through a 12-eV region that enclosed the double-excitation feature. The ratio of the intensity of the removed double-excitation peak to that of the white line for these samples was consistent with previous reports by Kodre *et al.* (46, 47).

Figure 2 shows the EXAFS spectra for selected cesium catalysts and compounds in this study, before removal of the double-excitation feature at about 5 $Å^{-1}$. Each of the compounds exhibited a similar looking EXAFS spectrum, with subtle differences in the shapes of the oscillatory peaks. The average Cs–O distances extracted from the cesium-modified zeolites were very similar to those of the bulk compounds, 2.94 ± 0.03 Å. This distance was comparable to 2.96 Å for Cs–O in cesium-exchanged ZSM-5 (48). The similarity in Cs–O distances allows us to inversely correlate the intensity of the white line region with coordination of cesium to oxygen, as discussed above. The narrow range in *k* space usable for the analysis prevented the reliable determination of coordination numbers and Debye–Waller factors. In summary, cesium was found to be more ionic when occluded in zeolite cages, as compared with bulk-phase compounds and cesium-exchanged zeolites.

FT-IR Spectroscopy of Chemisorbed Carbon Dioxide

The spectra obtained from adsorption of CO_2 at 373 K on NaX can be seen in Fig. 3. Bands located at 1484 and 1430 cm^{-1} are indicative of the formation of a true carbonate, which is produced when the negative charge is delocalized over the three oxygen atoms (2 from CO_2 and 1 from the zeolite framework) and stabilized by the electrostatic field of the Na cation (49). These bands, however, were not observed for other X zeolites in this study.

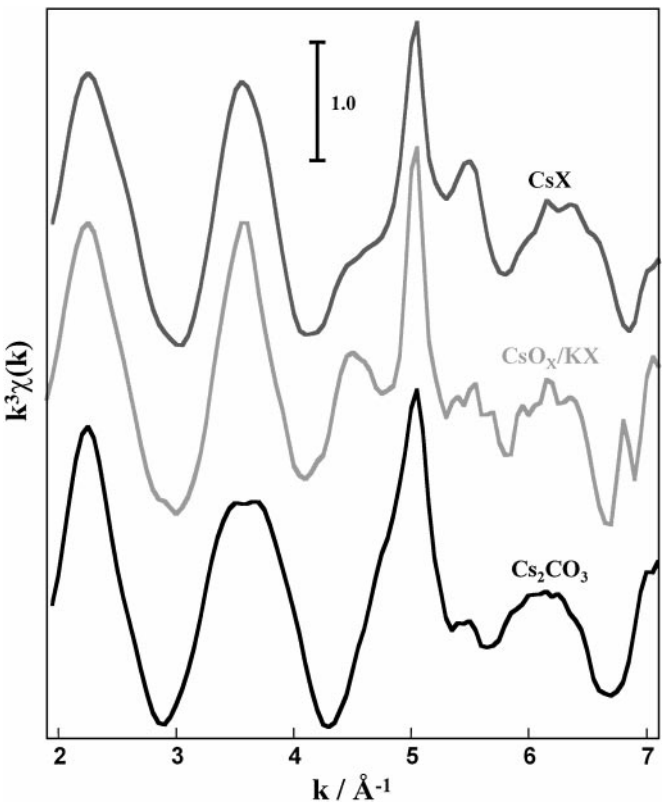

FIG. 2. Cs L_{III} edge EXAFS for CsO_x/KX, CsX, and Cs_2CO_3 at room temperature.

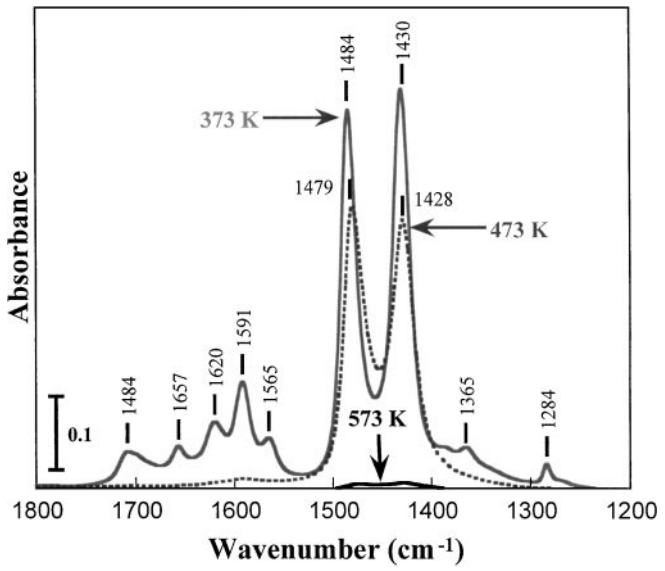

FIG. 3. FT-IR spectra of the carbonate region for chemisorbed species obtained on temperature-programmed desorption of CO_2 from NaX.

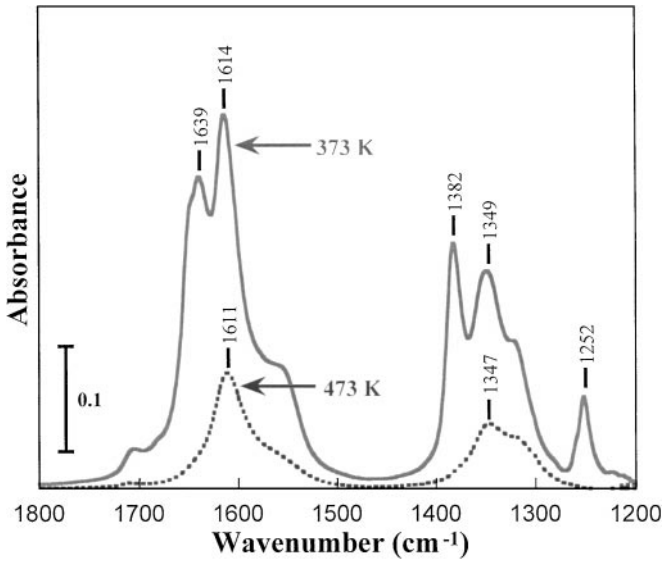

FIG. 5. FT-IR spectra of the carbonate region for chemisorbed species obtained on temperature-programmed desorption of CO_2 from CsX.

Apparently, larger cations have too low an electrostatic potential which results in greater covalent character (49). By using temperature-programmed desorption to remove the adsorbed species, the carbonates corresponding to bands in the range 1550–1700 cm^{-1} of the IR spectrum were completely removed after heating to 473 K, while those attributed to true carbonate were reduced. Almost all of the true carbonate species were removed by heating to 573 K in flowing helium.

The IR spectra for KX and CsX can be found in Figs. 4 and 5, respectively. Both of these zeolites exhibited bands consistent with the formation of bidenate carbonates, which typically have asymmetric stretching bands in the range 1610–1630 cm^{-1} and symmetric stretching bands in the range 1320–1340 cm^{-1}, to give an overall splitting of about 300 cm^{-1}. Unidentate carbonates, generally formed on strong base sites, typically exhibit asymmetric stretching bands in the range 1510–1560 cm^{-1} and symmetric stretching bands in the range 1360–1400 cm^{-1}, giving an overall splitting of about 150 cm^{-1}. At 373 K, adsorption of CO_2 on KX resulted in broadbands in the range 1620–1670 cm^{-1}, accompanied by bands in the range 1300–1350 cm^{-1}. Adsorption of CO_2 on CsX revealed similar bands which were slightly shifted toward that of a unidentate carbonate. Davydov *et al.* determined that a decrease in the splitting for bidentate carbonate toward band positions typical of unidentate carbonate corresponds to an increase in the basicity of the surface oxygen (50). The low wavenumber bands located between 1200 and 1260 cm^{-1} for both KX and CsX disappeared after heating to 473 K, indicating that those bands were not associated with the stronger basic centers on these zeolites, but rather with weakly bound species. After thermal desorption of weaker surface carbonate species from these two zeolites at 473 K, the KX sample contained bidentate carbonate bands of smaller splitting than CsX, indicating that KX had some stronger base sites than CsX. Complementary temperature-programmed desorption profiles for these alkali-exchanged zeolites, presented in Fig. 6, show that the peak CO_2 desorption temperature decreased with increasing electropositivity of the exchange cation. This observation has been made by Tsuji *et al.* for analogous X zeolites (4). One would expect stronger bases to exhibit higher desorption temperatures since greater energy would be needed to break

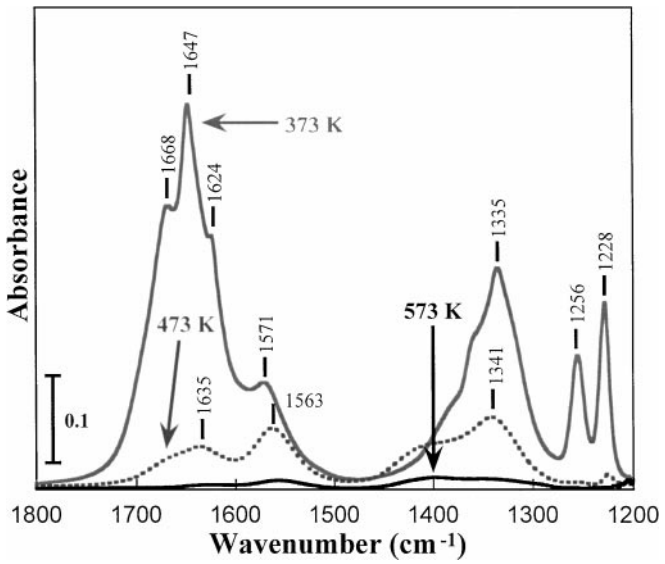

FIG. 4. FT-IR spectra of the carbonate region for chemisorbed species obtained on temperature-programmed desorption of CO_2 from KX.

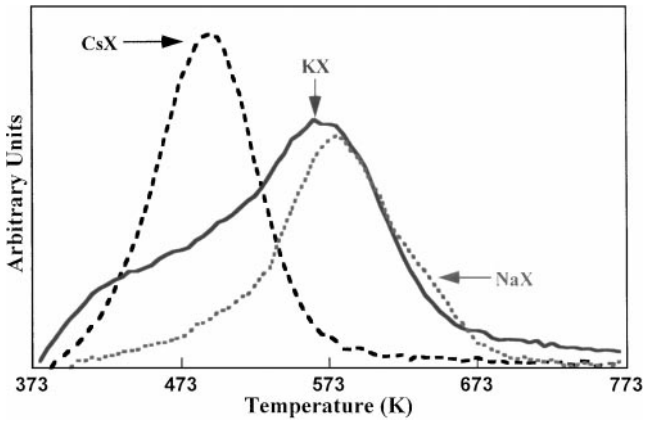

FIG. 6. Temperature-programmed desorption profiles of carbonate species from X zeolites after saturated adsorption at 373 K.

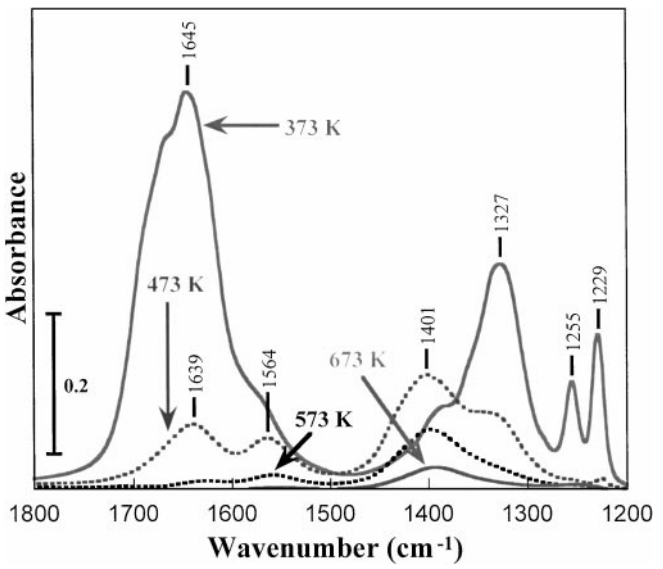

FIG. 7. FT-IR spectra of the carbonate region for chemisorbed species obtained on temperature-programmed desorption of CO_2 from CsO_x/KX.

the adsorbate–adsorbent interaction. Clearly, ranking base strength by comparing the desorption temperature of CO_2 is ambiguous because CO_2 adsorbs in different modes on the zeolites. Nevertheless, KX appeared to have stronger adsorption sites than CsX, which was also confirmed by IR spectroscopy. In addition, the presence of stronger sites on KX was consistent with results obtained from UV–vis studies of adsorbed iodine on these two zeolites (51). After heating to 573 K, all carbonate species were effectively removed from the CsX surface while a small amount remained on KX.

The IR spectra of carbon dioxide adsorbed on CsO_x/KX, presented in Fig. 7, exhibited a spectrum similar to that of KX at 373 K. This was presumably due to the fact that the occluded oxide did not greatly affect the basic sites found on the zeolite framework itself. On KX, complete desorption of CO_2 occurred by 673 K. However, unidentate carbonate bands were clearly visible at 673 K for CsO_x/KX and complete CO_2 desorption did not occur until the initial pretreatment temperature of 773 K was reached. Occluding cesium oxide species in KX zeolite created base sites stronger than those present on the parent zeolite.

Decomposition of 2-Propanol

The decomposition of 2-propanol was used as a probe reaction to investigate the effect of cesium loading on catalytic activity. The initial CsX used for these studies was washed only with water to eliminate the excess cesium remaining in the zeolite cages after ion exchange. It is generally accepted that dehydrogenation of 2-propanol to acetone occurs primarily over base catalysts while dehydration to propene occurs primarily over acid catalysts (52–55). Therefore, the reaction is a decent probe of the acid–base character of alkali oxide-loaded zeolites.

Reactivity results obtained after 2 h onstream are presented in Table 3. For CsX without any occluded cesium species located in the cages, the selectivity to acetone was only 9%, presumably due to the residual acidity of the ion-exchanged zeolite. The occlusion of only 1.3 CsO_x per unit cell resulted in a significant increase in the selectivity due primarily to a fourfold increase in the rate of acetone production. Loadings of 6.7 and 10.7 excess cesiums per unit cell further increased the selectivity to values of about 67 and 76%, respectively. The rate of acetone formation correlated linearly with the loading of cesium oxide over the range of Cs loadings investigated. Interestingly, the occlusion of CsO_x in the zeolite pores did not significantly affect

TABLE 3

Rates of 2-Propanol Reaction on CsX Zeolites Containing Occluded Cesium Oxide

Catalyst	Excess Cs per unit cell	Surface area ($m^2\ g^{-1}$)	Selectivity to acetone (%)	Rate of acetone formation ($\mu mol\ m^{-2}\ h^{-1}$)	Rate of propene formation ($\mu mol\ m^{-2}\ h^{-1}$)
CsX	0.0	513	9.0	0.3	3.0
CsO_x/CsX	1.3	454	32.3	1.2	2.5
CsO_x/CsX	6.7	383	67.4	6.8	3.3
CsO_x/CsX	10.7	344	76.4	11.2	3.5

TABLE 4

Physical Properties of Alkali Metal-Loaded Zeolite X Catalysts

Catalyst[a]	No. of excess alkali per supercage	Surface area ($m^2\ g^{-1}$)	Pore volume ($cm^3\ N_2\ g^{-1}$)
NaX[b]	0	879	0.330
NaN_3/NaX	2	742	0.282
NaN_3/NaX	4	473	0.180
CsN_3/NaX	2	639	0.245
CsN_3/NaX	4	426	0.161
KX[b]	0	783	0.293
NaN_3/KX	2	650	0.245
NaN_3/KX	4	418	0.157
CsN_3/KX	2	595	0.225
CsN_3/KX	4	335	0.128
CsX[b]	0	522	0.202
NaN_3/CsX	2	478	0.184
NaN_3/CsX	4	353	0.137
CsN_3/CsX	2	389	0.152
CsN_3/CsX	4	220	0.091

[a] After decomposition of the supported azide under vacuum.
[b] Heated to 573 K under vacuum.

the areal rate of propene production after incorporation of 10.7 excess Cs per unit cell, indicating that the supported species did not affect the residual acidity associated with the exchanged zeolite. This result contrasts our earlier findings for rubidium supported on classic metal oxide supports (56).

ESR Spectroscopy of Alkali Metal-Loaded X Zeolites

Electron spin resonance spectroscopy was used to investigate the electronic state of supported alkali species formed after thermal decomposition of supported alkali azides. The physical properties of the thermally treated materials can be found in Table 4. The reduction in pore volumes for the samples indicated that the alkali metal species reside in the pores of the zeolite and/or cause some destruction of the crystallinity. Figure 8 shows ESR spectra for these materials, with the g value for the DPPH standard given as a reference point (2.0036). In addition to the single lines present at about $g = 2.0$ for clusters formed within the zeolite cages, the decomposition of occluded azides resulted in broad ESR signals at g values near 2.08 for most samples, a feature that Martens *et al.* have attributed to alkali metal clusters in extralattice positions (17). Unfortunately, the elemental composition of these external metal clusters could not be determined; the clusters may contain a mixture of alkali metals obtained from either the azides or the exchange ions. Reported in Table 5 are the g values for the single lines characteristic of alkali clusters located within the zeolite cages.

The ESR spectrum for sodium azide decomposed on NaX showed a central line g value characteristic of the formation of Na clusters (19). However, as seen in Fig. 9, accurate determination of the g value was obtainable only for the $4NaN_3$/NaX (4 sodium azide molecules per NaX supercage) sample due to its higher peak intensity. The g values for the other azide-modified NaX zeolites were very near this value and assumed to be the same. The two spectra for CsN_3-modified NaX clearly indicated that cesium clusters were not present in the zeolite cages of these materials. Results from EDX analysis suggested that cesium species in $4CsN_3$/NaX migrated to the external surface of this material during azide decomposition. This segregation was likely enhanced due to the high loading of azide on the sample. Ionic clusters that exhibit hyperfine interactions in

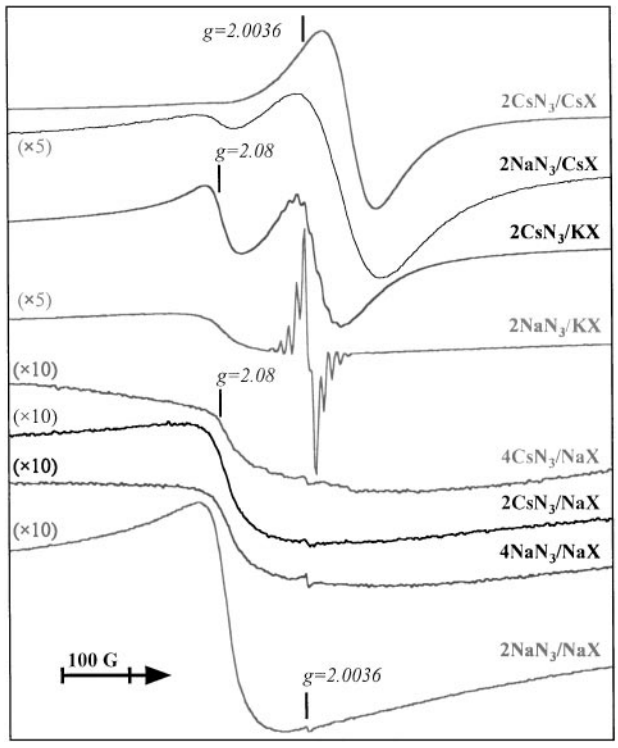

FIG. 8. ESR spectra at room temperature of alkali metal-modified X zeolites after decomposition of supported sodium and cesium azides.

TABLE 5

Room Temperature ESR g Values of Alkali Metal Particles in X Zeolites from Decomposition of Supported Azide

Supported azide per supercage	NaX	KX	CsX
$2NaN_3$	2.0023[a]	1.9995	1.9660
$4NaN_3$	2.0023	[b]	[b]
$2CsN_3$	2.0023[a]	1.9931	1.9660
$4CsN_3$	2.0023[a]	[b]	[b]

[a] Estimated.
[b] Not investigated using ESR.

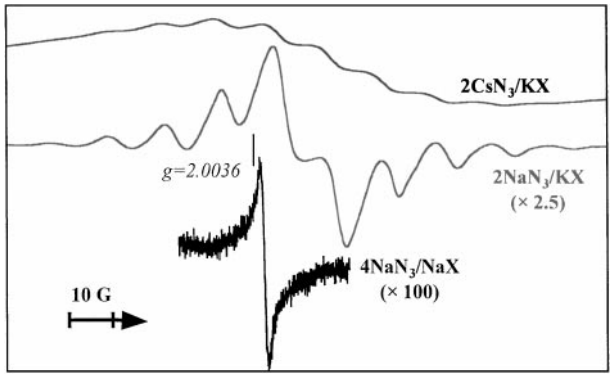

FIG. 9. Expanded ESR spectra of selected alkali metal-modified X zeolites.

ESR spectra were not seen on any of the azide-modified NaX zeolites, indicating that the slow decomposition procedure was successful in creating neutral Na clusters on the zeolite.

The location of the central line *g* value for the alkali metal-loaded KX zeolites indicated the formation of potassium clusters, despite the use of sodium and cesium azides as precursors. This result was also reported by Xu and Kevan for NaN_3 and CsN_3 decomposed on KX zeolite (19). Apparently, the zeolite cations exchanged with the impregnated alkali during either azide impregnation or thermal treatment. After azide decomposition, each of these KX samples exhibited a 10-line hyperfine interaction characteristic of a K_3^{2+} ionic cluster in addition to the central line characteristic of K-metal clusters (19, 23). The hyperfine interaction was more obvious for the sodium-loaded KX zeolite than the cesium-loaded one at identical alkali metal loadings. However, the NaN_3/KX zeolite appeared to contain both potassium and sodium clusters. Both of the KX zeolites also exhibited broad ESR lines at high *g* values, indicating the presence of additional extralattice alkali clusters.

The location of the central line *g* value for the alkali metal-loaded CsX zeolites indicated the formation of cesium metal clusters in the zeolite (19). Again, since sodium azide was impregnated on one of these samples, exchange with the original cesium cations located in CsX, during either catalyst preparation or thermal treatment, accounted for the formation of cesium metal. Xu and Kevan observed that cesium clusters were formed by the decomposition of any alkali azide in the presence of CsX (19). A broad feature indicative of extralattice metal clusters was also seen at high *g* values for $2NaN_3$/CsX but not for $2CsN_3$/CsX. Apparently, loading two cesium atoms per supercage of CsX prevented cesium from migrating to extralattice positions during decomposition of the occluded azide. Analysis by XPS on NaN_3/CsX and CsN_3/CsX confirmed that, unlike sodium, cesium did not preferentially migrate to the external surface (57).

Alkenylation of o-Xylene with 1,3-Butadiene

Several factors must be considered to synthesize an effective catalyst for the production of OTP from *o*-xylene and 1,3-butadiene. First, the *trans* isomer of 5-*o*-tolyl-2-pentene is more desirable than the *cis* isomer (26). Second, multiple alkenylations can take place at the side chain, thus decreasing the selectivity to OTP product. Also, alkenylation of the aromatic ring can occur on residual acid sites of the catalyst. Finally, 1,3-butadiene can oligomerize over strong base sites and deactivate the catalyst. Therefore, zeolites into which alkali metal had been incorporated in pores were investigated as potential catalysts that could enhance the selectivity and/or the relative rate to the *trans* form of the OTP product.

In this study, the following definition for selectivity is used (based on *o*-xylene conversion):

$$\text{selectivity} = \frac{\text{moles of OTP}}{\text{moles of mono-, di-, and trialkenylated products}}.$$

The side-chain alkenylation requires a strong base site to initiate the reaction. Preliminary reactions were performed by bubbling a pure 1,3-butadiene gas stream through a solution of bulk Na or K metal suspended in *o*-xylene. Over Na metal, no product was seen after 4 h, but 43% conversion of *o*-xylene was observed after 7 h. The color of the final solution was dark red, indicating the formation of organosodium intermediates in solution. Only a small spherical piece of Na metal was observed in the reactor at the end of 7 h. The overall selectivity was about 70% and the *trans*/*cis* ratio of OTP was 1.7, which was in agreement with the literature (26). The overall selectivity and *trans*/*cis* ratio observed over K metal (at lower conversion) were similar to those over Na. After the reaction was stopped, no piece of potassium metal was observed and the dark red color of the final solution indicated the presence of organopotassium intermediates. However, contrary to the Na metal case, reaction products were detected after only 0.5 h of reaction time. This faster reaction time, compared with reaction over Na metal, could be due to the fact that *o*-xylene can be directly metalated by K and not by Na (30). In both cases, a large amount of oligomerized butadiene was observed in the reactor after the reaction was stopped. A reduction in the partial pressure of 1,3-butadiene resulted in a reduction in the amount of oligomerized butadiene; therefore, subsequent reactions were performed using a dilute butadiene stream with a 1 : 9 ratio of 1,3-butadiene to dinitrogen.

A test of cesium oxide occluded in the pores of CsX (10.7 occluded cesium atoms per unit cell) did not show any activity for the alkenylation reaction, indicating the need for a metal site. Therefore, we focused on zeolites containing alkali metal species. Table 6 shows the reactivity results from the liquid-phase side-chain alkenylation of *o*-xylene

TABLE 6

Reactivity of *o*-Xylene + 1,3-Butadiene over Various Alkali Metal Catalysts[a]

Catalyst	No. of alkali metal per supercage	Trans/Cis	Selectivity[b] (%)	Conversion[c] (%)	Turnover number[d]
Na metal	0.005 g[e]	N/A	No reaction		0.0
NaN_3/NaX	2	0.9	86.4	3.9	5.5
NaN_3/NaX	4	1.0	86.2	3.8	2.8
CsN_3/NaX	2	0.8	94.0	4.0	6.3
CsN_3/NaX	4	2.1	89.9	13.9	12.3
K metal	0.008 g[e]	1.5	91.6	10.5[f]	43.3
NaN_3/KX	2	2.4	85.3	9.2	14.0
NaN_3/KX	4	2.4	91.8	1.5	1.2
CsN_3/KX	2	1.3	90.8	0.9	1.5
CsN_3/KX	4	N/A	No reaction		0.0
NaN_3/CsX	2	1.9	90.7	1.5	2.8
NaN_3/CsX	4	N/A	No reaction		0.0
CsN_3/CsX	2	N/A	No reaction		0.0

[a] Using a 1 : 9 butadiene : dinitrogen stream.
[b] OTP produced/sum of mono-, di-, and trialkenylated products.
[c] Conversion after 7.5 h of reaction time.
[d] Molecules of *o*-xylene converted after 7.5 h/theoretical number of alkali metal atoms present.
[e] Bulk alkali metal dispersed in *o*-xylene.
[f] Conversion is at 6.0 h.

with 1,3-butadiene over various alkali metal-supported zeolites after 7.5 h of reaction. For each alkali metal-modified zeolite, ring alkenylation accounted for about 3% of the total monoalkenylated product. Each active material was found to be catalytic since the ratio of the amount of *o*-xylene reacted to the theoretical amount of alkali metal present exceeded unity after a reaction time of 7.5 h (see Table 6). For each reaction in which 5-*o*-tolyl-2-pentene was detected, the solution was dark red, indicating that alkali metal formed from the decomposition of the supported azide leached into solution to form an organoalkali complex. Thus, catalytic activity was likely due to metal species both in the solution and associated with the zeolite. Nevertheless, the studies revealed interesting trends with regard to generating an active alkali species for alkenylation reactions.

Over a sodium-based catalyst, metalation of *o*-xylene at the benzylic position occurs via transmetalation from a butadiene–sodium adduct (30). Therefore, over Na catalysts, butadiene must undergo metalation before *o*-xylene can be activated. Sodium on NaX gave *trans*/*cis* ratios of 0.9 and 1.0 for initial loadings of two and four Na atoms per supercage, respectively, at a conversion of about 4%. In addition, these two catalysts exhibited similar selectivity and conversion profiles, as presented in Fig. 10. These *trans*/*cis* values are significantly lower than those observed by Dimitrov *et al.* for *o*-xylene alkenylation over other sodium-containing zeolite catalysts (26). The similar conversion profiles for the two NaN_3/NaX catalysts indicated that the higher loading of Na metal on the zeolite was not completely accessible to the reactants, possibly due to the formation of larger extralattice clusters, as suggested by ESR spectroscopy. The fact that the *trans*/*cis* ratio for $2NaN_3$/NaX was less than 1.0 indicated that the rate of *cis*-OTP production exceeded that of the *trans* isomer, which had not been seen previously. Although this result was quite interesting, the higher rate of formation for the *cis* isomer is not desired since the *trans* isomer is easier to convert to the final product. Reactivity over an amount of bulk sodium metal equivalent to that on the $2NaN_3$/NaX sample under identical reaction conditions resulted in no formation of alkenylation products after 7.5 h. However, alkenylation

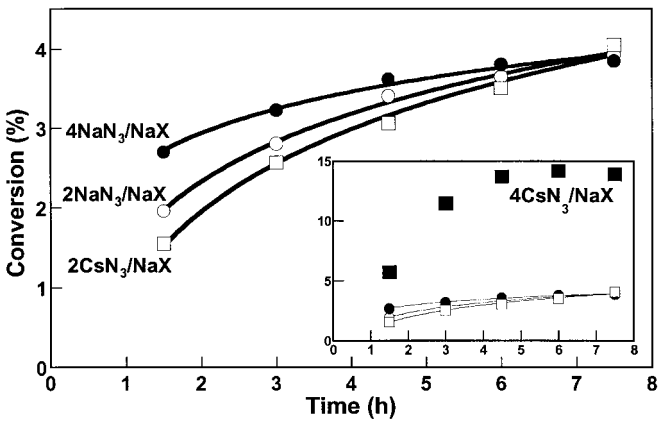

FIG. 10. Conversion of *o*-xylene over various alkali metal-loaded NaX zeolites.

did occur using a higher partial pressure of butadiene, as discussed above. This observation indicated that the high-surface-area zeolite supported sodium metal clusters capable of metalating 1,3-butadiene under dilute conditions, a process that was necessary for transmetalation to *o*-xylene and subsequent formation of OTP product.

Reactivity over catalysts prepared from the decomposition of two cesium azide molecules per supercage resulted in a *trans*/*cis* ratio less than 1.0 and a conversion profile similar to the Na analogue (see Fig. 10). Since ESR spectroscopy indicated the presence of Na metal clusters on the $2CsN_3$/NaX sample, the similarity in the reaction profiles was not surprising. However, the selectivity for $2CsN_3$/NaX was higher than that obtained from the $2NaN_3$/NaX catalyst. Increasing the Cs loading to four metal atoms per supercage resulted in a significant increase in the *trans*/*cis* ratio to 2.2. In addition, this sample was significantly more reactive than the other alkali-modified NaX zeolite samples. After 4.5 h, however, the conversion of *o*-xylene did not change for the $4CsN_3$/NaX sample due to deactivation of the catalyst.

The decomposition of two NaN_3 molecules per supercage on KX resulted in a catalyst that was more selective and reactive than NaX with a similar azide loading. Since ESR spectroscopy indicated that both Na and K clusters were present in the cages of the zeolite, the increase in reactivity could have possibly been due to the ability of potassium metal to directly metalate *o*-xylene, allowing for greater conversion compared with sodium (30). The conversion of *o*-xylene, presented in Fig. 11, significantly decreased when the amount of supported NaN_3 was increased from two to four molecules per KX supercage, a result that was contrary to observations on azide-modified NaX. As seen in Table 4, the high loading of NaN_3 significantly reduced the pore volume which may have inhibited access to or desorption from the active sites in the zeolite. Both of the NaN_3-modified KX catalysts showed similar *trans*/*cis* ratios, which were greater than those seen for identical loadings in NaX. The OTP product formed over $2CsN_3$/KX had a *trans*/*cis* ratio of 1.3, which was close to that seen over unsupported potassium metal, which according to ESR spectroscopy was present in the zeolite cages. A conversion profile for alkenylation over a piece of bulk K metal suspended in *o*-xylene is also pictured in Fig. 11. Alkenylation of *o*-xylene did not begin until after 3 h of bubbling dilute butadiene through refluxing *o*-xylene. However, once alkenylation started, the conversion increased rapidly with time, which was quite different from the conversion profiles of alkali-loaded KX zeolites. It is unclear at this time what role the K_3^{2+} ionic clusters have in affecting activity. The $4CsN_3$/KX catalyst was ineffective for the side-chain alkenylation of *o*-xylene with 1,3-butadiene, presumably due to steric constraints with this high loading of decomposed cesium azide. Indeed, there was a large reduction in pore volume for this sample.

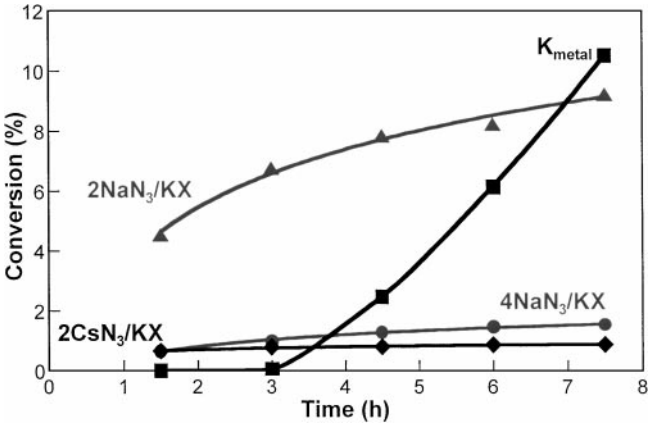

FIG. 11. Conversion of *o*-xylene over various alkali metal-loaded KX zeolites.

Decomposing two sodium azides per supercage of CsX resulted in a catalyst with reduced conversion compared with similar azide loadings on NaX and KX, possibly due to the smaller pore volume of CsX. Loading four sodium azide molecules per CsX supercage produced an inactive catalyst. Likewise, no reaction was seen for a loading of two Cs atoms per CsX supercage, which ESR spectroscopy showed to have no extraframework alkali metal clusters. Interestingly, the most active catalysts contained extraframework clusters detected by ESR spectroscopy. Perhaps it was these extralattice clusters that were responsible for the initiation of the alkenylation reaction.

CONCLUSIONS

We have used X-ray, IR, and ESR spectroscopy to probe the atomic and electronic structures around alkali elements in zeolite cages. Near-edge studies at the Cs L_{III} edge confirmed that the occluded cesium oxide species were in a 1+ formal oxidation state. In addition, analysis of the white line intensities from XANES showed that the occluded cesium atoms in zeolites were more ionic than cesium in bulk-phase compounds. Results from IR spectroscopy of adsorbed CO_2 confirmed the basic nature of occluded cesium oxide. Increasing the loading of occluded cesium oxide in the cages of CsX resulted in a linear increase in the areal rate of the base-catalyzed dehydrogenation of 2-propanol to acetone, whereas the areal rate of acid-catalyzed dehydration to propene remained relatively unaffected. Thus, even though the occluded species were strong bases, they did not effectively neutralize the residual acidity of the exchanged zeolite. Stronger base materials containing occluded alkali metal clusters were prepared by the decomposition of alkali azides impregnated in X zeolites. Electron spin resonance spectroscopy showed that the resulting occluded alkali species depended on the alkali present as the exchange cation instead of the alkali azide being decomposed.

Therefore, ion exchange during methanolic impregnation or azide decomposition must have taken place between the azide and the zeolite. Extralattice metal clusters were evident on each of the alkali metal-loaded zeolites, except $2CsN_3$/CsX. Most of the alkali-metal loaded zeolites were effective catalysts for the side-chain alkenylation of *o*-xylene with 1,3-butadiene to form 5-*o*-tolyl-2-pentene. However, the inactivity of $2CsN_3$/CsX suggested that extralattice metal clusters might be the active species for the reaction.

ACKNOWLEDGMENTS

This work was supported by the Department of Energy (Basic Energy Sciences, Grant DEFG05-95ER14549). Research was carried out in part at the National Synchrotron Light Source, Brookhaven National Laboratory, which is supported by the U.S. Department of Energy, Division of Materials-Sciences and Division of Chemical Sciences (DOE Contract DE-AC02-76CH00016). Helpful discussions with Rutger van Santen and Matthew Neurock are also acknowledged.

REFERENCES

1. Pines, H., Vesely, J. A., and Ipatieff, N. N., *J. Am. Chem. Soc.* **77**, 347 (1955).
2. Hathaway, P. E., and Davis, M. E., *J. Catal.* **116**, 263 (1989).
3. Corma, A., Fornes, V., Martin-Aranda, R. M., Garcia, H., and Primo, J., *Appl. Catal.* **59**, 237 (1990).
4. Tsuji, H., Yagi, F., Hattori, H., and Kita, H., *Stud. Surf. Sci. Catal.* **75**, 1171 (1992).
5. Barthomeuf, D., *Catal. Rev. Sci. Eng.* **38**, 521 (1996).
6. Wieland, W. S., Davis, R. J., and Garces, J. M., *J. Catal.* **173**, 490 (1998).
7. Tsuchiya, S., Takase, S., and Imamura, H., *Chem. Lett.*, 661 (1984).
8. Tsuji, H., Yagi, F., and Hattori, H., *Chem. Lett.*, 1881 (1991).
9. Rodriguez, I., Cambon, H., Brunel, D., Lasperas, M., and Geneste, P., *Stud. Surf. Sci. Catal.* **78**, 623 (1993).
10. Kim, J. C., Li, H.-X., Chen, C.-Y., and Davis, M. E., *Microporous Mater.* **2**, 413 (1994).
11. Lasperas, M., Cambon, H., Brunel, D., Rodriguez, I., and Geneste, P., *Microporous Mater.* **7**, 61 (1996).
12. Rodriguez, I., Cambon, H., Brunel, D., and Lasperas, M., *J. Mol. Catal. A* **130**, 195 (1998).
13. Hunger, M., Schenk, U., Burger, B., and Weitkamp, J., *Angew. Chem. Int. Ed. Engl.* **36**, 2504 (1997).
14. Yagi, F., Kanuka, N., Tsuji, H., Nakata, S., Kita, H., and Hattori, H., *Microporous Mater.* **9**, 229 (1997).
15. Krawietz, T. R., Murray, D. K., and Haw, J. F., *J. Phys. Chem. A* **102**, 8779 (1998).
16. Martens, L. R. M., Grobet, P. J., and Jacobs, P. A., *Nature* **315**, 568 (1985).
17. Martens, L. R. M., Grobet, P. J., Vermeiren, W. J. M., and Jacobs, P. A., *Stud. Surf. Sci. Catal.* **28**, 935 (1986).
18. Xu, B., and Kevan, L., *J. Chem. Soc. Faraday Trans.* **87**, 2843 (1991).
19. Xu, B., and Kevan, L., *J. Phys. Chem.* **96**, 2642 (1992).
20. Brock, M., Edwards, C., Förster, H., and Schröder, M., *Stud. Surf. Sci. Catal.* **84**, 1515 (1994).
21. Hannus, I., Kiricsi, I., Beres, A., Nagy, J. B., and Forster, H., *Stud. Surf. Sci. Catal.* **98**, 81 (1995).
22. Beres, A., Hannus, I., and Kiricsi, I., *J. Therm. Anal.* **46**, 1301 (1996).
23. Xu, B., Chen, X., and Kevan, L., *J. Chem. Soc. Faraday Trans.* **87**, 3157 (1991).
24. Park, Y. S., Lee, Y. S., and Yoon, K. B., *Stud. Surf. Sci. Catal.* **84**, 901 (1994).
25. Puskas, I., U.S. Patent 4,034,052 (1977).
26. Dimitrov, C., Popova, Z. I., and Thyong, F. V., *Compt. Rend. Acad. Bulg. Sci.* **33**, 353 (1980).
27. Fushimi, N., Inamasa, K., and Takagawa, M., U.S. Patent 5,344,806 (1994).
28. Takagawa, M., Inamasa, K., Fushimi, N., Hashimoto, A., and Sasaki, T., U.S. Patent 5,444,172 (1995).
29. Takagawa, M., Kato, K., Fushimi, N., and Kedo, K., U.S. Patent 5,436,381 (1995).
30. Eberhardt, G. G., and Peterson, H. J., *J. Org. Chem.* **30**, 82 (1964).
31. Matsumoto, T., Kumagai, Y., and Kumata, F., U.S. Patent 5,625,102 (1997).
32. Morse, P. M., *C&EN* **75**, 8 (1997).
33. Pines, H., Vesely, J. A., and Ipatieff, V. N., *J. Am. Chem. Soc.* **77**, 554 (1955).
34. Pines, H., and Mark, V., *J. Am. Chem. Soc.* **78**, 4316 (1956).
35. Schaap, L., and Pines, H., *J. Am. Chem. Soc.* **79**, 4967 (1957).
36. Pines, H., and Schaap, L. A., *Adv. Catal.* **12**, 117 (1960).
37. Pines, H., and Sih, N. C., *J. Org. Chem.* **30**, 280 (1965).
38. Pines, H., and Oszczapowicz, J., *J. Org. Chem.* **32**, 3183 (1967).
39. Ewald, P. P., and Hermann, C., "Strukturbericht 1913–1926," p. 73, 1926.
40. Kemner, K. M., Hunter, D. B., Elam, W. T., and Bertsch, P. M., *J. Phys. Chem.* **100**, 11698 (1996).
41. Helms, A., and Klemm, W., *Z. Anorg. Allg. Chem.* **242**, 33 (1939).
42. Tsai, K.-R., Harris, P. M., and Lassettre, E. N., *Phys. Rev.* **60**, 338 (1952).
43. Wyckoff, R. W. G., "Crystal Structures," p. 170. Wiley, New York, 1963.
44. Purans, J., Kuzmin, A., and Burrattini, E., *Jpn. J. Appl. Phys.* **32**, 64 (1993).
45. Strobel, P., Durr, J., Tullier, M.-H., and Charenton, J.-C., *J. Mater. Chem.* **3**, 453 (1993).
46. Kodre, A., Arcon, I., Hribar, M., Stuhec, M., Villain, F., and Parent, P., *J. Phys. IV* **4**, C9/397 (1994).
47. Kodre, A., Arcon, I., Hribar, M., Stuhec, M., Villain, F., Drube, W., and Troger, L., *Physica B* **208/209**, 379 (1995).
48. Esemann, H., Forster, H., Geidel, E., and Krause, K., *Microporous Mater.* **6**, 321 (1996).
49. Jacobs, P. A., van Cauwelaert, F. H., and Vansant, E. F., *J. Chem. Soc. Faraday Trans. 1* **69**, 2130 (1973).
50. Davydov, A. A., Shepot'ko, M. L., and Budneva, A. A., *Kinet. Katal.* **35**, 299 (1994).
51. Doskocil, E. J., Bordawekar, S. V., Kaye, B. G., and Davis, R. J., *J. Phys. Chem. B* **103**, 6277 (1999).
52. Yashima, T., Suzuki, H., and Hara, N., *J. Catal.* **33**, 486 (1974).
53. Ai, M., *Bull. Chem. Soc. Jpn.* **50**, 2579 (1977).
54. Zaki, M. I., and Sheppard, N., *J. Catal.* **80**, 114 (1983).
55. Gervasini, A., and Auroux, A., *J. Catal.* **131**, 190 (1991).
56. Doskocil, E. J., Bordawekar, S. V., and Davis, R. J., *J. Catal.* **169**, 327 (1997).
57. Bordawekar, S. V., and Davis, R. J., *J. Catal.*, in press.